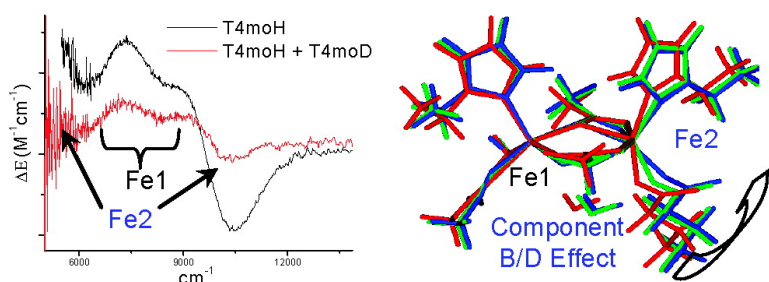Article

Geometric and Electronic Structure Studies of the Binuclear Nonheme Ferrous Active Site of Toluene-4-monooxygenase: Parallels with Methane Monooxygenase and Insight into the Role of the Effector Proteins in O Activation

Jennifer K. Schwartz, Pin-pin Wei, Kevin H. Mitchell, Brian G. Fox, and Edward I. Solomon

More About This Article

Additional resources and features associated with this article are available within the HTML version:

- Supporting Information
- Links to the 2 articles that cite this article, as of the time of this article download
- Access to high resolution figures
- Links to articles and content related to this article
- Copyright permission to reproduce figures and/or text from this article

View the Full Text HTML

Geometric and Electronic Structure Studies of the Binuclear Nonheme Ferrous Active Site of Toluene-4-monooxygenase: Parallels with Methane Monooxygenase and Insight into the Role of the Effector Proteins in O₂ Activation

Jennifer K. Schwartz,[†] Pin-pin Wei,[†,‡] Kevin H. Mitchell,[§] Brian G. Fox,*,[§] and Edward I. Solomon*,[†]

Department of Chemistry, Stanford University, Stanford, California 94305, and Department of Biochemistry, College of Agricultural and Life Sciences, University of Wisconsin, Madison, Wisconsin 53705

Received January 26, 2008; E-mail: bgfox@biochem.wisc.edu; edward.Solomon@stanford.edu

Abstract: Multicomponent monooxygenases, which carry out a variety of highly specific hydroxylation reactions, are of great interest as potential biocatalysts in a number of applications. These proteins share many similarities in structure and show a marked increase in O₂ reactivity upon addition of an effector component. In this study, circular dichroism (CD), magnetic circular dichroism (MCD), and variable-temperature, variable-field (VTVH) MCD have been used to gain spectroscopic insight into the Fe(II)Fe(II) active site in the hydroxylase component of Toluene-4 monooxygenase (T4moH) and the complex of T4moH bound by its effector protein, T4moD. These results have been correlated to spectroscopic data and density functional theory (DFT) calculations on MmoH and its interaction with MmoB. Together, these data provide further insight into the geometric and electronic structure of these biferrous active sites and, in particular, the perturbation associated with component B/D binding. It is found that binding of the effector protein changes the geometry of one iron center and orientation of its redox active orbital to accommodate the binding of O₂ in a bridged structure for efficient 2-electron transfer that can form a peroxo intermediate.

Introduction

The family of multicomponent monooxygenases includes methane monooxygenases, phenol hydroxylases, α/β-alkene monoxygenases, and the four-component alkene/aromatic monooxygenases. Each member can selectively oxidize different hydrocarbons at a nonheme diiron active site within the hydroxylase component, which must couple with an effector protein for optimal turnover. Crystallographic and spectroscopic studies of these and other binuclear nonheme iron enzymes have shown that there is a strong conservation in the structural motif of the diiron active site (e.g., soluble methane monooxygenase, ribonucleotide reductase, stearoyl-acyl carrier protein Δ^9 desaturase).[1–11] This binuclear motif consists of two irons bridged by a set of carboxylate ligands with an additional carboxylate and histidine ligand bound to each iron. Despite similarities at the active site, these enzymes perform a wide variety of chemical reactions with dioxygen. Some examples include oxygen activation for substrate oxygenation, desaturation, and oxidation.[12–14] Because of the catalytic relevance of these reactions in medicine and industry, there has been significant effort directed toward elucidating structure/reactivity correlations over these enzymes.

One of the more heavily studied members of this family is soluble methane monooxygenase (sMMO). The hydroxylase component (MmoH) of this enzyme converts methane to methanol through reaction with O₂. From crystallography, the reduced form of the MmoH active site (Figure 1) is found to contain two inequivalent irons separated by 3.3 Å.[5] The irons are bridged by two carboxylate ligands: Glu144 in a $\mu-1,3$ fashion and Glu243 in a $\mu-1,1$ fashion. These bridging

[†] Stanford University.

[‡] Present address: Department of Pathology, University of Cambridge, Cambridge CB2 1QP, United Kingdom.

[§] University of Wisconsin.

(1) Pulver, S.; Froland, W. A.; Fox, B. G.; Lipscomb, J. D.; Solomon, E. I. *J. Am. Chem. Soc.* **1993**, *115*, 12409–12422.

(2) Yang, Y. S.; Broadwater, J. A.; Pulver, S. C.; Fox, B. G.; Solomon, E. I. *J. Am. Chem. Soc.* **1999**, *121*, 2770–2783.

(3) Pulver, S. C.; Tong, W. H.; Bollinger, J. M., Jr.; Stubbe, J.; Solomon, E. I *J. Am. Chem. Soc.* **1995**, *117*, 12664–12678.

(4) Wei, P. P.; Skulan, A. J.; Mitic, N.; Yang, Y. S.; Saleh, L.; Bollinger, J. M.; Solomon, E. I. *J. Am. Chem. Soc.* **2004**, *126*, 3777–3788.

(5) Whittington, D. A.; Lippard, S. J. *J. Am. Chem. Soc.* **2001**, *123*, 827–838.

(6) Elango, N.; Radhakrishnan, R.; Froland, W.; Wallar, B.; Earhart, C.; Lipscomb, J.; Ohlendorf, D. *Protein Sci.* **1997**, *6*, 556–568.

(7) Rosenzweig, A. C.; Nordlund, P.; Takahara, P. M.; Frederick, C. A.; Lippard, S. J. *Chem. Bio.* **1995**, *2*, 409–418.

(8) Yang, Y. S.; Baldwin, J.; Ley, B. A.; Bollinger, J. M., Jr.; Solomon, E. I. *J. Am. Chem. Soc.* **2000**, *122*, 8495–8510.

(9) Strand, K. R.; Yang, Y. S.; Andersson, K. K.; Solomon, E. I. *Biochemistry* **2003**, *42*, 12223–12234.

(10) Lindqvist, Y.; Huang, W.; Schneider, G.; Shanklin, J. *Embo J.* **1996**, *15*, 4081–4092.

(11) Logan, D.; Su, X.; Aberg, A.; Regnstrom, K.; Hajdu, J.; Eklund, H.; Nordlund, P. *Structure* **1996**, *4*, 1053–1064.

(12) Feig, A. L.; Lippard, S. J. *Chem. Rev.* **1994**, *94*, 759–805.

(13) Solomon, E. I.; Brunold, T. C.; Davis, M. I.; Kemsley, J. N.; Lee, S. K.; Lehnert, N.; Neese, F.; Skulan, A. J.; Yang, Y. S.; Zhou, J. *Chem. Rev.* **2000**, *100*, 235–349.

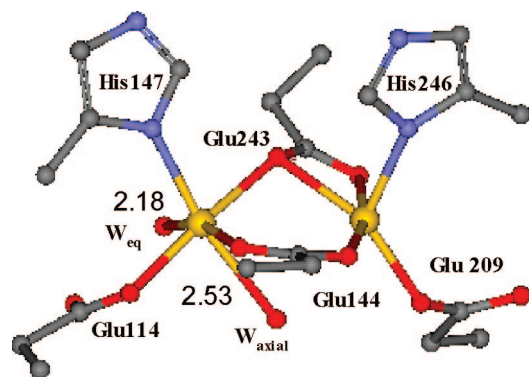(14) Baik, M. H.; Newcomb, M.; Friesner, R. A.; Lippard, S. J. *Chem. Rev.* **2003**, *103*, 2385–2420.

A R T I C L E S

Figure 1. Schematic representation of the active site of reduced MmoH from crystal structure 1FYZ; Fe−water bond distances are labeled in angstroms. Amino acid sequences show that the same active site ligands are present in T4moH.

carboxylates each provide one ligand to Fe1 in addition to His147, monodentate Glu114, and two weakly bound waters, making Fe1 6-coordinate. The Fe2 environment is 5 coordinate, consisting of bidentate ligation from the bridging Glu243, and monodentate coordination from Glu144, Glu209, and His246. Different protomers solved within the reduced MmoH crystal structures have shown only a single water bound to Fe1 and this remains an issue between crystallographic and spectroscopic data (vide infra).[1,5,7]

Although MmoH alone is capable of slow turnover with methane,[15] its rate and mechanism are strikingly different when bound by the effector protein MmoB. The addition of MmoB to MmoH leads to a 1000-fold increase in its dioxygen reactivity, as well as a different distribution of products and build up of different intermediates.[16−19] This indicates that even though MmoB contains no metal and has no catalytic activity by itself, it plays an important role in the turnover of MmoH. Crystal structures of Phenol Hydroxylase (PHH) in complex with its regulatory protein (PHM) show that PHM binds in the canyon region formed between the three protomers of PHH, approximately 12 Å above the active site.[20] Modeling of the MmoH-MmoB complex,[21] which has been attempted based on crystal and solution structures of MmoB[17,22] and MmoB mutant studies,[23−25] suggests a similar binding site. This location could allow the effector protein to regulate entrance of dioxygen and various substrates into the binuclear iron center, accounting for the high degree of selectivity exhibited by the monoxygenases.[17,25,26] A second role for component B, supported by CD/MCD studies, is a structural perturbation at the active site that alters the

geometry of one of the irons and allows for a stronger interaction with the substrate.[27,28]

Many similarities have been noted between sMMO and other multicomponent monooxygeanses, in particular toluene-4-monooxygenase (T4MO). T4MO, from *Pseudomonas mendocina* KR1, is a four-component alkene/aromatic monooxygenase that oxidizes toluene to *p*-cresol in 96 % purity.[29] It has been studied in the bioremediation of petroleum spills[30] and as a biocatalyst for selective aromatic ring hydroxylation.[31−34] T4MO consists of a 211-kDa hydroxylase (T4moH), a 36-kDa NADH oxidoreductase (T4moF), a 12.5-kDa Rieske-type [2Fe-2S] ferredoxin (T4moC), and an 11.6-kDa effector protein (T4moD). T4moD plays a parallel role to MmoB, as its interaction with the hydroxylase component changes the reactivity of the diiron center, and the product distributions observed from certain substrates.[29,35] Mutation studies involving the hydroxylase[34] and coupling components[36] again support a possible role for the effector protein in regulating access to the active site. While the overall amino acid sequence identity between MmoH and T4moH is small,[37] the essential amino acid residues near their diiron centers are conserved. Thus descriptions of the T4moH diiron center and the effect of T4moD on this site would provide further insight into how structural changes within the diiron site affect reactivity in the multicomponent monooxygenases and other nonheme diiron enzymes.

In this study, the biferrous centers in T4moH and the T4moH/T4moD complex are investigated using a combination of near-IR circular dichroism (CD), magnetic circular dichroism (MCD) and variable-temperature, variable-field (VTVH) MCD. CD/MCD spectroscopies provide a direct probe of the geometric and electronic structure of each iron of the biferrous enzyme in solution, and VTVH MCD determines ground-state magnetic properties reflecting bridging ligation between the irons. To gain further insight into the structures of the active sites of T4moH and MmoH, a series of density functional calculations were performed on the reduced structure of MmoH to correlate the crystallography to the spectroscopy of both proteins. These calculations provide insight into the spectroscopic features of T4moH and MmoH and a more complete description of their ligand fields, as well as the spectral perturbation that occurs upon binding of their effector proteins. The results define

(15) Andersson, K. K.; Froland, W. A.; Lee, S. K.; Lipscomb, J. D. *New J. Chem.* **1991**, *14*, 411−415.

(16) Wallar, B. J.; Lipscomb, J. D. *Biochemistry* **2001**, *40*, 2220−2233.

(17) Chang, S. L.; Wallar, B. J.; Lipscomb, J. D.; Mayo, K. H. *Biochemistry* **2001**, *40*, 9539−9551.

(18) Liu, K. E.; Nesheim, J. C.; Lee, S.-K.; Lipscomb, J. D. *J. Biol. Chem.* **1995**, *270*, 24662−24665.

(19) Lipscomb, J. D.; Que, L. *J. Biol. Inorg. Chem.* **1998**, *3*, 331−336.

(20) Sazinsky, M. H.; Bard, J.; Di Donato, A.; Lippard, S. J. *J. Biol. Chem.* **2004**, *279*, 30600−30610.

(21) Brazeau, B. J.; Wallar, B. J.; Lipscomb, J. D. *Biochem. Biophys. Res. Commun.* **2003**, *312*, 143−148.

(22) Chang, S. L.; Wallar, B. J.; Lipscomb, J. D.; Mayo, K. H. *Biochemistry* **1999**, *38*, 5799−5812.

(23) Zhang, J.; Wallar, B. J.; Popescu, C. V.; Renner, D. B.; Thomas, D. D.; Lipscomb, J. D. *Biochemistry* **2006**, *45*, 2913−2926.

(24) Zhang, J.; Lipscomb, J. D. *Biochemistry* **2006**, *45*, 1459−1469.

(25) Brazeau, B. J.; Lipscomb, J. D. *Biochemistry* **2003**, *42*, 5618−5631.

(26) Brazeau, B. J.; Wallar, B. J.; Lipscomb, J. D. *J. Am. Chem. Soc.* **2001**, *123*, 10421−10422.

(27) Pulver, S.; Froland, W.; Lipscomb, J.; Solomon, E. *J. Am. Chem. Soc.* **1997**, *119*, 387−395.

(28) Mitic, N.; Schwartz, J. K.; Brazeau, B.; Lipscomb, J. D.; Solomon, E. I. manuscript in preparation.

(29) Mitchell, K. H.; Studts, J. M.; Fox, B. G. *Biochemistry* **2002**, *41*, 3176−3188.

(30) Park, J.; Johnson, D. R.; Abriola, L. M.; Kukor, J. J. *Abstracts of the General Meeting of the American Society for Microbiology*, 102nd General Meeting of the American Society for Microbiology, Salt Lake City, UT, May 19−23, 2002; American Chemical Society: Washington, DC, 2002; p 402.

(31) Tao, Y.; Fishman, A.; Bentley, W.; Wood, T. K. *J. Bacteriol.* **2004**, *186*, 4705−4713.

(32) McClay, K.; Fox, B. G.; Steffan, R. J. *Appl. Environ. Microbiol.* **2000**, *66*, 1877−1882.

(33) Pikus, J. D.; Studts, J. M.; McClay, K.; Steffan, R. J.; Fox, B. G. *Biochemistry* **1997**, *36*, 9283−9289.

(34) Moe, L. A.; Hu, Z.; Deng, D.; Austin, R. N.; Groves, J. T.; Fox, B. G. *Biochemistry* **2004**, *43*, 15688−15701.

(35) Fox, B. G. L. Y.; Dege, J. E.; Lipscomb, J. D. *J. Biol. Chem.* **1991**, *266*, 540−550.

(36) Orville, A. M.; Studts, J. M.; Lountos, G. T.; Mitchell, K. H.; Fox, B. G. *Acta Crystallogr. Sect. D: Biol. Crystallogr.* **2003**, *D59*, 572−575.

(37) Coufal, D. E.; Blazyk, J. L.; Whittington, D. A.; Wu, W. W.; Rosenzweig, A. C.; Lippard, S. J. *Eur. J. Biochem.* **2000**, *267*, 2174−2185.

geometric and electronic structural similarities between the active sites of T4moH and MmoH, including the structural changes associated with effector protein binding that greatly enhance O_2 reactivity.

Experimental Section

Sample Preparation. MOPS buffer (Sigma), deuterium oxide (99.9 atom % D, Aldrich), sodium dithionite (Sigma), and glycerol (98% D, Cambridge Isotope Laboratories) were commercially purchased and used as obtained. Deuterated buffer was degassed with 99.9% pure argon; glycerol was degassed by heating under vacuum overnight and then subjected to 10 freeze−pump−thaw cycles at 10^{-3} Torr.

T4moH and T4moD were expressed and purified as previously reported.[38] The degassed iron(III)-loaded protein was fully reduced in deuterated buffer with 1 μL of 5 mM methyl viologen and 10−15 μL of 30 mM dithionite (final concentration: 1.8−2 mM dithionite) for CD. T4moD was added to T4moH until the CD spectrum no longer changed. The final molar ratio of T4moH (protomer) to T4moD was 1:1. The final pH of each sample was 7.3. Protein samples were prepared for MCD in the same way as for CD with an additional step of mixing the protein with 60% (v/v) glycerol-d_6 until homogeneous to create a suitable glass. From CD studies, the glycerol was found to have no effect on the biferrous site. The samples were then immediately frozen in liquid nitrogen. The protein samples were prepared and loaded into the sample holders in an inert atmosphere.

CD and MCD Spectroscopy. CD studies were performed on a JASCO J200D spectropolarimeter operating with a liquid nitrogen-cooled InSb detector in the 560−2000 nm region. Low-temperature MCD and VTVH MCD data were acquired on this spectropolarimeter, modified to accommodate an Oxford Instrument SM4000 7T-superconducting magnet capable of magnetic fields up to 7.0 T and temperatures down to 1.6 K. Protein samples prepared for MCD studies were slowly inserted into the cryostat to reduce strain in the resulting optical glass.

The CD and MCD spectra were fit using a constrained nonlinear least-squares procedure in order to find the minimum number of ligand field transitions required to simultaneously fit both spectra. Each spectroscopic method has a different selection rule; thus, transitions can have different intensities and signs but similar energies. CD is taken at 278 K whereas MCD is taken at much lower temperatures (4 K). Therefore, bands in MCD can slightly shift in energy and sharpen relative to those in CD.

VTVH MCD data (MCD intensity at a specific wavelength as a function of temperature and applied magnetic field) were fit with a model consisting of a series of non-Kramers doublets[39] using a simplex routine that minimizes the χ-squared value. A goodness of fit parameter (χ-square/number of float parameters) was utilized in the comparison of different fit results. The $g_{||}$ values of the ground and excited sublevels as well as the energies obtained give information concerning the spin states and bridging of the dimer. In addition, a spin-projection model[13] was applied to confirm the results obtained from the doublet model and identify the specific Fe(II) center of the dimer associated with the ligand field transition being studied by VTVH MCD. This procedure is described in the results section.

Density Functional Calculations. Electronic structure calculations (geometry optimization and single point) were carried out with the Jaguar 6.0 package. Coordinates were obtained from the RCSB Protein Data Bank (1FYZ),[5] from which the active site model of reduced MmoH was approximated by truncating each of the coordinating ligands (E209, H246, E243, E144, H147, E114, WAT492, WAT1230), and replacing their α carbon with a methyl

group. The position of each α carbon was then frozen to mimic protein backbone constraints. Second sphere hydrogen bonding residues were replaced by formate and ammonia molecules, which were also frozen during optimization.[40] The model was optimized using unrestricted BP86,[41,42] with Slater local exchange, and Vosko-Wilk-Nusair local correlation,[43] which has been previously shown to work well for diiron systems.[4,44] For initial optimizations, the iron atoms were described by the LACVP** basis set,[45] atoms within 3 bonds of iron used 6−31G*, and all other atoms used 6−31G. Final coordinates of the active site model were obtained by energy minimization using the default geometry optimization criteria of Jaguar 6.0.[46] Single point energies of all final structures were calculated using triple-ζ basis sets for all atoms (LACV3P** for iron atoms, 6−311G* for atoms within 3 bonds of iron, and 6−311G on all other atoms). Orbital occupation Tables were generated using *QMForge.*[47] Complete coordinates of all final geometry-optimized models can be found in the Supporting Information.

Results and Analysis

I. Spectroscopy. A. CD and Low-Temperature MCD Spectroscopy. NIR, CD, and MCD spectra for reduced T4moH are shown in Figure 2, with the Gaussian fit of the data shown in
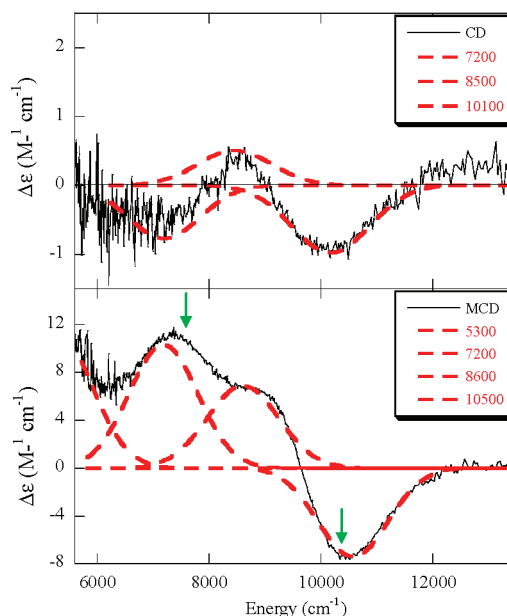

Figure 2. (Top) CD spectrum of T4moH, recorded at 5 °C and (Bottom) MCD spectrum of T4moH, recorded at 1.6 K and 7 T. The experimental data (black line) are fit to the individual Gaussian band shapes (red line). Green arrows indicate where VTVH data were collected.

(38) Studts, J. M.; Mitchell, K. H.; Pikus, J. D.; McClay, K.; Steffan, R. J.; Fox, B. G. *Protein Expression Purif.* **2000**, *20*, 58–65.

(39) Solomon, E. I.; Pavel, E. G.; Loeb, K. E.; Campochiaro, C. *Coord. Chem. Rev.* **1995**, *144*, 369–460.

(40) The hydrogen bonding residues were truncated to the smallest reasonable models providing similar hydrogen bonding interactions as observed in the protein. These were Asp242 and Asp143 as formates, CHO_2^-; Gln140 as ammonia, NH_3; water1231 and water963. The positions of the heavy atoms (C,N,O) were frozen along with the positions of hydrogens replacing carbon atoms.

(41) Becke, A. D. *J. Chem. Phys.* **1986**, *84*, 4524.

(42) Perdew, J. P. *J. Chem. Phys.* **1986**, *33*, 8822.

(43) Vosko, S. H.; Wilk, L.; Nusair, M. *Can. J. Phys.* **1980**, *58*, 1200.

(44) Skulan, A. J.; Hanson, M. A.; Hsu, H. F.; Que, L.; Solomon, E. I. *J. Am. Chem. Soc.* **2003**, *125*, 7344–7356.

(45) Hay, P.; Wadt, W. *J. Chem. Phys.* **1985**, *82*, 299–310.

(46) Geometry convergence criteria were: change in total energy, $\Delta E <$ $5e^{-5}$ hartree, maximum local energy gradient, $\delta E/\delta S < 4.5e^{-4}$ hartree/ Å, $\delta E/\delta S$(RMS) $< 3e^{-4}$ hartree/Å, $\Delta S < 1.8e^{-3}$ Å, ΔS(RMS) $< 1.2e^{-3}$ Å.

(47) Tenderholt, A. L. *QMForge*, Version 2.1; http://qmforge.sourceforge. net.
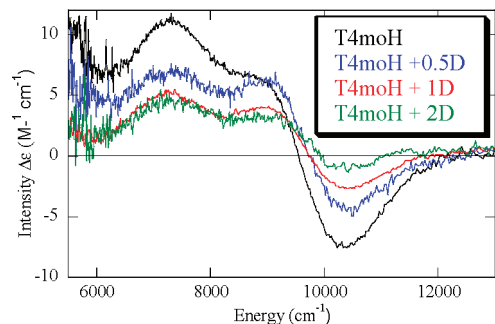
Figure 3. MCD titration of T4moH with T4moD. Recorded at 5 °C with 0 (black), 0.5 (blue), 1 (red), and 2 (green) molar equivalents of T4moD effector protein per protomer ($\alpha\beta\gamma$) of T4moH.

red. The CD spectrum (Figure 2, top) is comprised of one positive transition at 8500 cm^{-1} and two negative transitions at 7200 and 10 100 cm^{-1}. The MCD spectrum (Figure 2, bottom) shows a large negative peak at 10 500 cm^{-1} and three positive peaks, which can be fit at 5300, 7200, and 8600 cm^{-1}. No further transitions are visible up to the protein absorbance at 280 nm. The four distinct peaks of T4moH reflect two inequivalent Fe(II) centers, as a single ferrous ion can only give rise to two peaks in the near-IR region.[48] The two peaks around 10 000 cm^{-1} separated by 2000 cm^{-1} may be assigned as a six-coordinate iron center, but this assignment would require the remaining bands at 5300 and 7200 cm^{-1} to be assigned as a distorted 4C center, as 5C sites require a transition near 10 000 cm^{-1}.[13] Alternatively, two inequivalent 5C iron sites would also be consistent with the energies of the four transitions (one higher and one lower energy transition for each Fe). These possibilities will be distinguished in the VTVH MCD results and analysis section.

Titration of T4moH with T4moD leads to a dramatic change in the CD and MCD spectra. One T4moD was required per binuclear unit to fully saturate these spectral changes. Further addition of T4moD produced no significant change. Since the perturbations in CD were difficult to discern due to the low signal-to-noise ratio, an MCD titration of T4moH with T4moD was also performed (Figure 3). The MCD titration reveals a clear decrease in intensity of the peaks at 5300 cm^{-1} and 10000 cm^{-1} with the addition of T4moD, however these bands are still present even after addition of excess T4moD, as is more clearly confirmed by the corresponding CD spectrum (Figure 4, top). In addition, peak positions of all bands have shifted slightly in energy. Simultaneous Gaussian-fits of the CD and MCD spectra of T4moD bound to T4moH are shown in Figure 4. The CD spectrum (Figure 4, top) can be fit with a negative band at 6900 cm^{-1}, and positive bands at 9100 and 10 500 cm^{-1}, and the MCD spectrum (Figure 4, bottom) of T4moH+ T4moD is best fit with bands at 5500, 7100, 9000, and 10 600 cm^{-1}. These peak energies again reflect two inequivalent Fe(II) centers in the binuclear site.

B. VTVH MCD Spectroscopy. The MCD intensities of reduced T4moH and T4moH+T4moD increase as temperature decreases, indicating that all transitions for both species are MCD C-terms associated with paramagnetic doublet ground states that are split by a magnetic field. Variable temperature-variable field saturation data were taken at 7350 and 10 400 cm^{-1} for T4moH (green arrows in Figure 2 MCD) and are

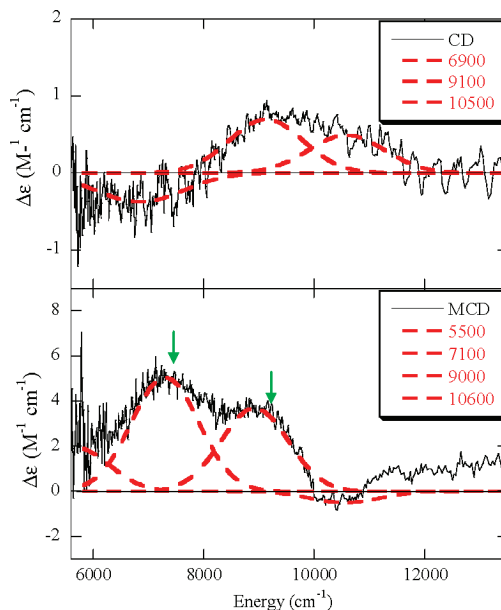(48) Pavel, E.; Kitajima, N.; Solomon, E. *J. Am. Chem. Soc.* **1998**, *120*, 3949–3962.

Figure 4. (Top) CD spectrum of T4MOH + T4MOD, recorded at 5 °C and (Bottom) MCD spectrum of T4MOH + T4MOD, recorded at 1.6 K and 7 T. The experimental data (black line) are fit to the individual Gaussian band shapes (red line).
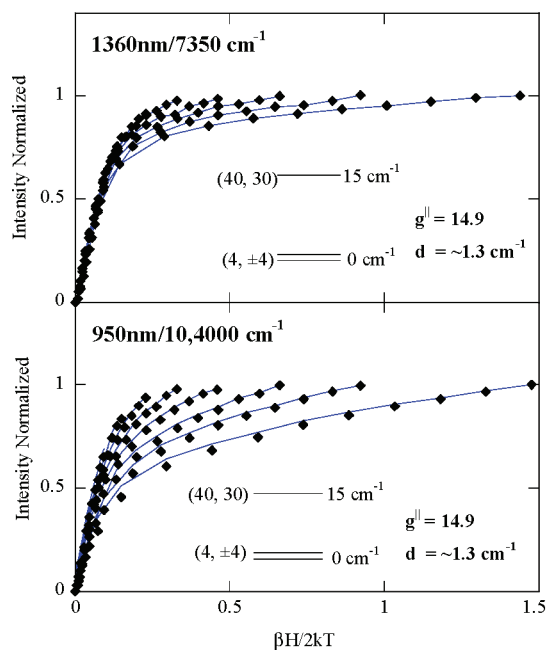

Figure 5. VTVH MCD of T4MOH at (top) 7350 cm^{-1} and (bottom) 10 400 cm^{-1} (green arrows in Figure 2) with their respective fits included. Fit parameters given in Table 1.

shown in Figure 5. These energy positions were chosen to minimize overlap between transitions. The low signal-to-noise ratio at the 5500 cm^{-1} peak prevented the collection of a satisfactory data set for this transition. Both sets of VTVH MCD curves are nested, with the high-temperature data offset from the low-temperature data when the isotherms are plotted as a function of $\beta H/2kT$. This is characteristic of low lying excited states and the rhombic zero-field splitting (ZFS) of a non-Kramers doublet ground state, which leads to nonlinear field-induced mixing between the sublevels of the doublet[13] The VTVH MCD data for the two bands do not overlay within standard deviation. This could arise from different polarizations

Table 1. MCD Fit Parameters Obtained for the Ground State and Lowest Excited State(S) of Reduced T4moH and T4moH + D[a]

transition	T4moH	T4moH + T4moD	MmoH	MmoH + MmoB
	7350 cm^{-1}	7350 cm^{-1}	7750 cm^{-1}	7750 cm^{-1}
δ_1 (cm^{-1})	1.3	0.7	<1	<1
g	14.9	15.9	14.7	16.2
E (1st ES) (cm^{-1})	15	7	7	5
g	0	0	0	0
E (2nd ES) (cm^{-1})	x	x	10	12
g	x	x	12	12
J (cm^{-1})	+0.9−1.2	+0.9−1.3	+0.2−0.4	+0.3−0.5
D_1 (cm^{-1})	−5.0 < D < −1	−9.0 < D < −3	−5.0 < D < −1	−9.0 < D < −3
D_2 (cm^{-1})	−10.0 < D < −6	−9.0 < D < −3	−10.0 < D < −3	−6.0 < D < −4

[a] Data of MmoH and MmoH+MmoB from ref 3 are included for comparison. A mark of x indicates that the addition of a second excited state did not improve the fit.

if the transitions are on the same iron, or if the two ligand field transitions are localized on the two different Fe(II) centers.

The VTVH MCD data of the reduced binuclear nonheme active site were analyzed using two complementary models. The first is a doublet model for non-Kramers systems, which uses a linear *B*-term to accommodate the second-order Zeeman effect from the field induced mixing between different doublets. The ground-state parameters obtained are then analyzed using a spin-Hamiltonian. The second method, a spin-projection model, calculates the dimer wave functions based on the fact that the MCD intensity is proportional to the spin-expectation values of the iron center being studied by VTVH MCD projected on the dimer wave functions. These are described below.

In a non-Kramers system, the VTVH MCD data are fit using the MCD intensity expression below (eq 1).[39,49−51]

$$\Delta\varepsilon = \sum_i \left[(A_{sat\lim})_i \left(\int_0^{\pi/2} \frac{\cos^2\theta \sin\theta}{\Gamma_i} g_{\|i}\beta H\alpha_i d\theta - \sqrt{2}\frac{M_z}{M_{xy}} \int_0^{\pi/2} \frac{\sin^3\theta}{\Gamma_i} g_{\perp i}\beta H\alpha_i d\theta \right) + B_i H\gamma_i \right] \quad (1)$$

where

$$\Gamma_i = \sqrt{\delta_i^2 + (g_{\|i}\beta H\cos\theta)^2 + (g_{\perp i}\beta H\sin\theta)^2}$$

$$\alpha_i = \frac{\exp[-(E_i - \Gamma_i/2)/kT] - \exp[-(E_i + \Gamma_i/2)/kT]}{\sum_j \exp[-(E_j - \Gamma_j/2)/kT] + \exp[-(E_j + \Gamma_j/2)/kT]}$$

$$\gamma_i = \frac{\exp[-(E_i - \delta_i/2)/kT] + \exp[-(E_i + \delta_i/2)/kT]}{\sum_j \exp[-(E_j - \beta_j/2)/kT] + \exp[-(E_j + \delta_j/2)kT]}$$

$(A_{sat\lim})_i$, B_i, δ_i, $g_{\|i}$, and $g_{\perp i}$ are the *C*-term and *B*-term MCD intensity, the rhombic ZFS, and the dimer g values of the *i*th doublet, respectively. E_i is the energy of the *i*th sublevel, and the energy of the ground state is defined as zero. The Boltzmann population over all states has been included in both the *C*-term and the *B*-term intensities as the factors α_i and γ_i respectively. *H* is the applied magnetic field, *k* is the Boltzmann constant, and M_z and $M_{x,y}$ are the transition dipole moments for the directions indicated.

The lowest temperature (1.6 K) data collected at 7350 cm^{-1} for T4moH (black diamonds in Figure 5, top) were fit using eq 1 by floating the $A_{sat\lim}$, *B*, δ, and $g_{\|}$ while fixing $g_{\perp}$ and the

(49) Stevens, P. J. *Annu. Rev. Phys. Chem.* **1974**, *25*, 201−232.
(50) Zhang, Y.; Gebhard, M. S.; Solomon, E. I. *J. Am. Chem. Soc.* **1991**, *113*, 5162−5175.
(51) Bennet, D. E.; Johnson, M. K. *Biophys. Acta.* **1987**, *911*, 71−80.
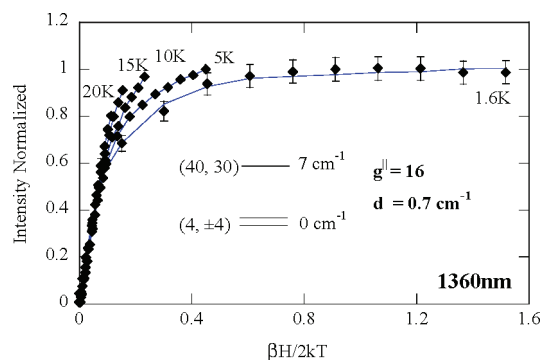
Figure 6. VTVH MCD of T4MOH+T4MOD at 7350 cm^{-1} (green arrow in Figure 4) with the best fit included; 3 K and 7 K curves were not included for visual clarity. Fit parameters given in Table 1.

polarization ratio $M_z/M_{x,y}$ at zero. Allowing $g_{\perp}$ and $M_z/M_{x,y}$ to float individually did not improve the fits. The best fit to the complete data set requires a single non-Kramers doublet with $g_{\|} \approx 16$ and $\delta \approx 1.3$ cm^{-1}, indicating that the ground state is $M_s = \pm 4$. Fits using other values of $g_{\|}$ were poor (graphically and goodness of fit). This is consistent with the EPR data.[38] Two excited singlets 15 cm^{-1} above the ground state are required to fit the higher-temperature saturation data. Inclusion of a third excited state does not have a significant effect on the fitting results. A good fit for the 10 400 cm^{-1} band of T4moH (Figure 5, bottom) gives, within error, the same set of ground and excited states (Table 1), indicating that both transitions arise from the same ground state. Included for comparison in Table 1 are the results for MmoH.

Similar VTVH MCD measurements and analyses were performed on the 7350 cm^{-1} band of T4moH + T4moD (arrows in Figure 4), which are shown in Figure 6 with the fit values in Table 1. VTVH data at 9000 cm^{-1} overlaid within standard deviation of the VTVH data from the 7350 cm^{-1} band. VTVH MCD data could not be collected at the 5500 or 10 500 cm^{-1} bands due to poor signal-to-noise ratios. Analysis of the VTVH MCD data gives a best fit with $g_{\|} \approx 16$ and $\delta \approx 0.7$ cm^{-1}, indicating that the ground state is again $M_s = \pm 4$. Two excited singlets 7 cm^{-1} above the ground state were required in order to fit the higher-temperature saturation data in Figure 6. Inclusion of a higher excited state did not have a significant effect on the fitting results. Thus upon binding of T4moD to T4moH, the ground-state spin of the biferrous site remains $M_{s\_tot} = \pm 4$, but the energy separation of the ground to the first excited state decreases.

A high-spin ferrous ion has an $S = 2$ ground state with $M_s = 0, \pm 1$, and ± 2. This 5-fold degeneracy will split due to zero-field splitting (ZFS) defined by the spin Hamiltonian parameters,

D (axial) and E (rhombic). In an exchange coupled system, the two ferrous ions can interact through bridging ligands to give $S_{tot} = S_1 + S_2|...|S_1 - S_2 = 4, 3, 2, 1$ and 0 levels. These levels are split by the exchange coupling $H = -2JS_1S_2$ to generate $(2S_{tot} + 1)$ M_{s_tot} degenerate levels. Since the magnitude of D and J are comparable in binuclear nonheme ferrous systems, their combined effects need to be considered.

Equation 2 gives the expression for the spin-Hamiltonian of a biferrous system,[13] which operates on the uncoupled basis set $|S_1, S_2, M_{s1}, M_{s2}\rangle$, where the subscripts indicate the two ferrous centers:

$$H = -2J\hat{S}_1 \cdot \hat{S}_2 + D_1(\hat{S}^2_{z1} - 1/3S(S+1)) + E_1(\hat{S}^2_{x1} - \hat{S}^2_{y1}) +$$
$$D_2(\hat{S}^2_{z2} - 1/3S(S+1)) + E_2(\hat{S}^2_{x2} - \hat{S}^2_{y2}) + g_{z1}\beta H_z\hat{S}_{z1} +$$
$$g_{x1}\beta H_x\hat{S}_{x1} + g_{y1}\beta H_y\hat{S}_{y1} + g_{z2}\beta H_z\hat{S}_{z2} + g_{x2}\beta H_x\hat{S}_{x2} + g_{y2}\beta H_y\hat{S}_{y2}$$
$$(2)$$

Here, J is the exchange coupling, D_1, D_2, E_1, and E_2 are the axial and rhombic ZFS parameters, and H is the magnetic field. Zeeman terms ($g_{z1}\beta H_{z1}S_{z1}$...etc.) are also included, where the g value can be coupled to the ZFS parameters using ligand field theory as given in eqs 2a and 2b. λ is the Fe(II) ground-state spin−orbit coupling constant ($\sim$100 cm^{-1}), k^2 is the Stevens orbital reduction factor, that is, ($|k| < 1$), and accounts for the effects of covalency.

$$D_{Fe^{2+}} = \frac{-k^2\lambda}{4}(g_{xFe^{2+}} + g_{yFe^{2+}} - 2g_{zFe^{2+}}) \quad (2a)$$

$$E_{Fe^{2+}} = \frac{-k^2\lambda}{4}(g_{yFe^{2+}} - g_{xFe^{2+}}) \quad (2b)$$

Diagonalization of a 25 × 25 matrix describing the interaction of the M_{si} (i = Fe1, Fe2) sublevels as functions of J and D_i and E_i in zero magnetic field gives the wave functions of the binuclear ferrous spin states and their energies, which are dependent on the relative magnitudes and signs of the exchange coupling and the ZFS. The magnitude of the D's are constrained to be less than 15 cm^{-1} (the largest value observed in model systems and obtained from ligand field calculations); the maximum E/D value is 1/3 by definition. From Table 1, T4moH has a ground state with $M_s = \pm 4$ ($g = 16$) and a lowest excited state consisting of two singlets. This situation occurs when the two D_i's are negative and J is positive. A spin Hamiltonian analysis of these data gives a J-value for T4moH of $+1.0 \pm 0.2$ cm^{-1}, indicating a ferromagnetically coupled system. Analysis of the VTVH MCD fit parameters (bottom of Table 1) give inequivalent D_1 and D_2 ranging from -9 to -3 cm^{-1}. Application of this protocol to T4moH+T4moD results in similar parameters relative to those of T4moH. However, in contrast to T4moH, T4moH+T4moD was found to have more equivalent ZFS values ($D_1 \approx D_2 \approx -5.3$ cm^{-1}).

In the above VTVH MCD analysis for T4moH and T4moH+T4moD, Zeeman contributions between sublevels were included using an empirical B-term in the MCD intensity expression (B_i in equation 1). The data can alternatively be fit with the spin-Hamiltonian wave functions from equation 2 where MCD intensity is proportional to the spin-expectation values of the single iron center being studied by MCD projected onto the dimer states. Thus, depending on the values of D_1, E_1, D_2, and E_2, it is sometimes possible to identify which iron center in the binuclear site is associated with the MCD transition being studied (as well as the polarization of that transition).[13]

The best spin-Hamiltonian fits to the VTVH MCD data for T4moH taken at 7350 cm^{-1} are included in Figure 7. The data
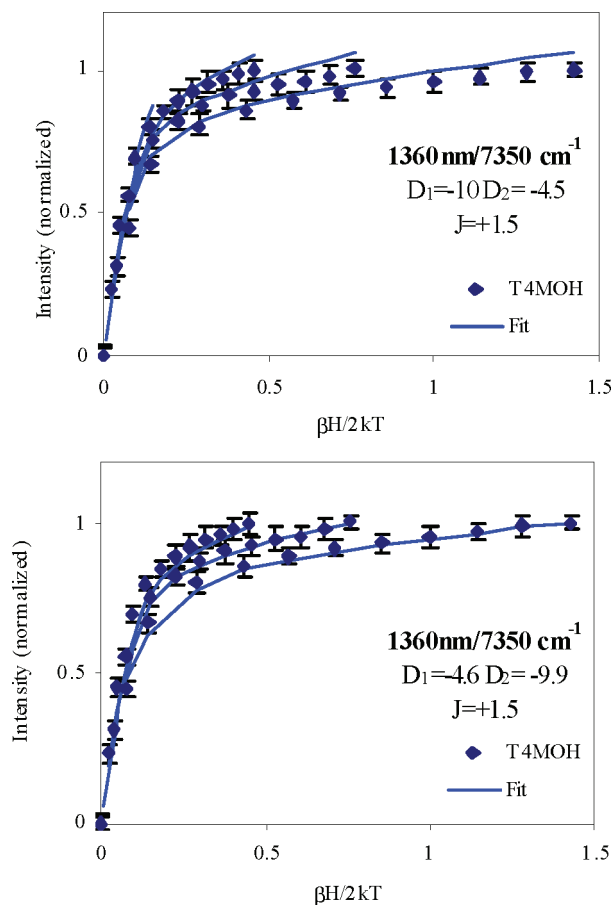

Figure 7. Spin-Hamiltonian fits to the T4MOH VTVH MCD data taken at 7350 cm^{-1}. The top graph is a fit with D_1 as the larger negative value and the bottom graph is D_1 as the smaller negative value.

were fit with a positive J value of 1.5 cm^{-1} and D_1 (the iron on which the transition is centered) was tested with a value of either -5 or -10 cm^{-1}. The data at 7350 cm^{-1} show that this band is better fit with the smaller negative D value (Figure 7 bottom vs top) although this fit is not definitive. A fit to the 10400 cm^{-1} saturation data for T4moH found that D_1 must be the larger negative D value for a good fit (Figure 8 top vs bottom). This reflects the fact that the 10 400 cm^{-1} data show a large difference in the nesting behavior in comparison with the data at 7350 cm^{-1}. This analysis, coupled with the observed band perturbations in the T4moD titration, allows these transitions to be assigned to different iron centers. This procedure could not be performed for T4moH+T4moD, as D_1 and D_2 are too close in value.

Returning to the possibility of a 6C+4C biferrous site raised earlier, the ligand field transition at 7500 cm^{-1} could reflect either a 5C or 4C center. Ligand field calculations show that distorted tetrahedral 4C Fe(II) sites have a d_z^2 ground state, which requires the zero-field splitting to be positive. The VTVH data for both T4moH and T4moH+T4moD could not be fit with a positive D value, eliminating the possibility of the two low energy bands being associated with a 4C Fe(II).[1,52] Thus from the CD, MCD, and VTVH MCD data and analysis, the reduced form of T4moH contains a 5C,5C diiron center, with the peaks at 7200 and 8600 cm^{-1} being associated with one iron and the 5300 and 10 500 cm^{-1} transitions associated with the second
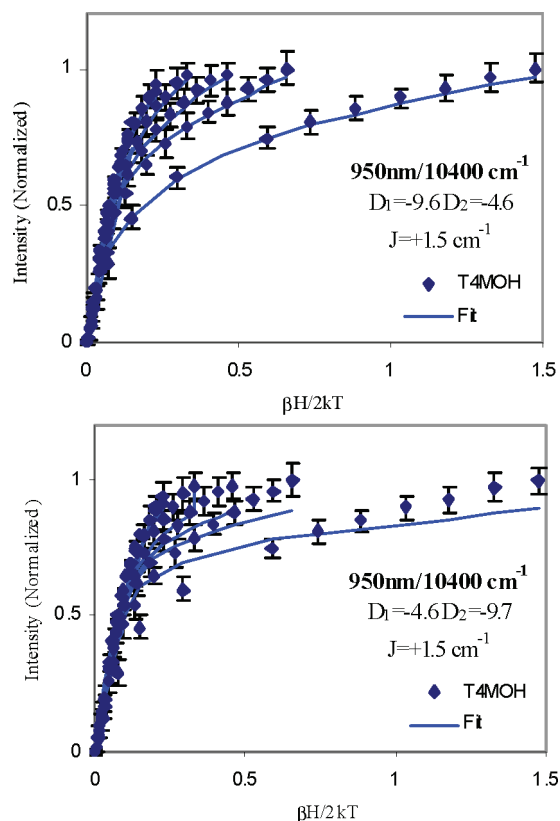
(52) Varret, F.; Hartmann-Boutron, F. *Ann. Phys.* **1968**, *3*, 157–168.

Figure 8. Spin-Hamiltonian fits to the T4MOH VTVH MCD data taken at 10400 cm^{-1}. The top graph is a fit with D_1 as the larger negative value and the bottom graph is D_1 as the smaller negative value.

iron. This assignment is further confirmed by the titration with T4moD, which only perturbs the bands at 5300 and 10 500 cm^{-1} assigned to the second iron center. T4moH has a ground state of $M_s = \pm 4$ with two excited singlets 15 cm^{-1} above the ground state. Both the doublet-fit and the spin-Hamiltonian fit find that T4moH has a weak ferromagnetic coupling J value of 1.5 cm^{-1} indicating the presence of an orthogonal exchange pathway typical of a $\mu-1,1$ carboxylate bridge.

Addition of T4moD shifts the low energy transition at 5300 up to 5500 cm^{-1} and changes its intensity along with the intensity of the 10 500 cm^{-1} MCD transition. Both transitions are assigned to one iron center. Transitions at 7200 cm^{-1} and 8500 cm^{-1}, associated with the other iron, remain relatively unperturbed. These assignments are consistent with the spin-Hamiltonian analysis of the T4moH VTVH MCD, which finds that the transitions at 7200 and 10 500 cm^{-1} belong to the two different iron centers. VTVH MCD data of T4moH+T4moD show the ground state remains $M_s = \pm 4$ with two excited singlets, which have decreased in energy to 7 cm^{-1} above the ground state. The diiron center in the T4moH+T4moD complex remains ferromagnetically coupled with negative D_1 and D_2, however the D values become closer in magnitude. Thus, addition of T4moD to T4moH leads to the distortion of one iron, with its ZFS parameter D becoming more similar in magnitude to that of the other iron. These results parallel those from the CD/MCD data of MmoH and MmoH+MmoB[27] in which one of the two ferromagnetically coupled 5 coordinate irons observed in the hydroxylase component is perturbed upon binding by the effector protein.

II. Calculations. A. Geometry Optimization of Reduced MmoH. 1. Comparison to Spectroscopy. To gain further insight into the resting structures of T4moH and MmoH as well as the
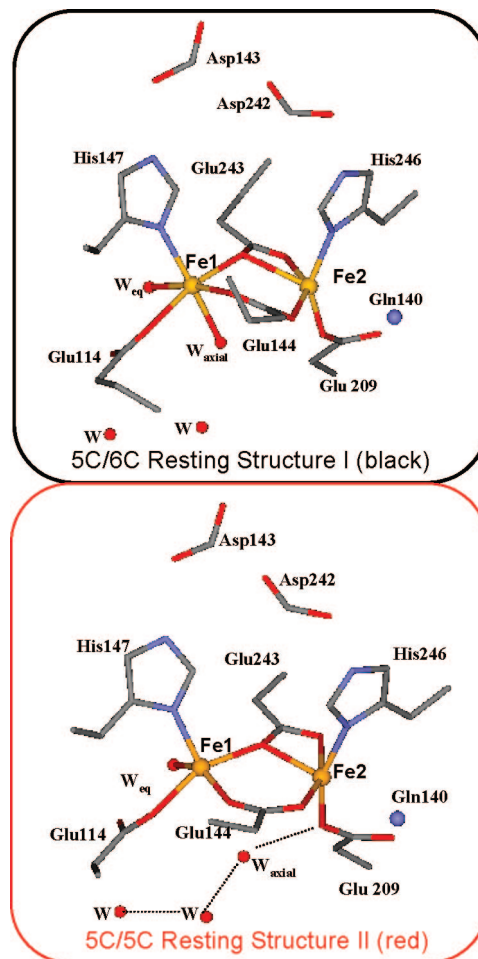
Figure 9. (Top) Geometry optimized Structure I of diiron active site in reduced MmoH with one 6-coordinate and one 5-coordinate Fe. (Bottom) Optimized resting structure II in which axial water dissociates from Fe1, leaving two 5-coordinate Fe's. The dashed lines at the bottom represent the hydrogen bonding network formed between the waters.

possible structural changes associated with the binding of T4moD/MmoB, computational studies were carried out on the reduced structure of MmoH. Coordinates for the active site were taken from the PDB file (1FYZ), and the truncated model was energy minimized (Figure 9A top). In Resting Structure I obtained from the initial optimization, one 5 coordinate iron and one 6 coordinate Fe are bridged in a $\mu-1,3$ fashion by Glu144 and in a $\mu-1,1$ fashion by Glu243 as found in the crystal structure. By determining the total energy difference between the HS ($M_s = 4$) and BS ($M_s = 0$) states of this structure, an estimation of the ground-state exchange coupling constant was also made using equation 3:[53]

$$J = -(E_{HS} - E_{BS})/S^2_{max} \qquad (3)$$

The calculated energies for this structure give a value of $J \approx +2$ cm^{-1}, consistent with the weak ferromagnetic coupling ($\lesssim +1$ cm^{-1}) determined by VTVH MCD analysis.[1] This reflects the $\mu-1,1$ bridge found in the optimized structure.

The bridging Glu243 coordinates to Fe2 in a bidentate mode. (Note: here Fe1 and Fe2 refer to the irons as labeled in Figure 9, which will be correlated to the irons described by the VTVH MCD analysis below.) Monodentate coordination from Glu144 (the second bridging carboxylate), His 246, and Glu209 complete its distorted trigonal bypyramidal ligand field. Cal-

Table 2. Bond Lengths and Energies from DFT Geometry Optimizations of the MmoH Active Site[a]

bond (Å) or angle (deg)	6C/5C resting I	5C/5C resting II	5C/5C resting III	5C/5C + MmoB IV
Fe1−N (His147)	2.21	2.14	2.07	2.07
Fe1−O (Glu114)	2.17	2.15	2.18	2.16
Fe1−O (Glu144)	2.04	2.07	2.03	2.02
Fe1−O$_b$ (Glu243)	2.19	2.18	2.22	2.25
Fe1−O (W$_{eq}$)	2.18	2.12	2.06	2.11
Fe1−O (W$_{axial}$)	2.31	2.90	3.7	3.80
Fe2−N (His246)	2.09	2.08	2.09	2.17
Fe2−O (Glu209)	1.95	2.00	1.99	1.98
Fe2−O (Glu144)	2.08	2.12	2.11	2.11
Fe2−O (Glu243)	2.36	2.28	2.26	2.18
Fe2−O$_b$ (Glu243)	2.20	2.19	2.21	2.15
Fe−Fe-Glu209	111	94.5	114	135
ΔE (kcal/mol)	0	−7	−1.5	+7.5

[a] O$_b$ refers to the bridging oxygen of Glu243.

Table 3. Fe−Water Bond Distances (Å) in Selected Crystal Structures of Reduced MmoH from RCSB Protein Data Bank

PDB structure ID	W$_{eq}$	W$_{axial}$
1MTY: left Prot	2.08	2.67
1MTY: right Prot	2.63	1.92
1FYZ: Prot A	2.49	2.38
1FYZ: Prot B	2.18	2.53

culated bond lengths are given in Table 2. Fe1 is ligated by a single oxygen from each of the bridging carboxylates, Glu243 and Glu144, a terminal carboxylate Glu114, and His147. Additionally, there are two waters bound to Fe1: W$_{eq}$ at 2.18Å and W$_{axial,}$ more weakly bound at 2.31 Å. The water bound directly across from His147 is labeled axial and the equatorial labeled water is bound opposite Glu144 on Fe1 (Figure 9, top). Because the spectroscopy of these proteins shows two inequivalent 5 coordinate irons and rules out a 5 + 6 coordinate site, it was necessary to further probe the binding of the water molecules.

Inspection of the active sites in multiple crystal structures of MmoH reveals that Fe-Water distances vary from about 1.9 to 2.7 Å, showing Fe1 to be 5 or 6 coordinate (Table 3).[53,54] This variability in the Fe−W bond distances suggest that one or both waters are either very weakly coordinated or not bound to Fe1. Single point calculations varying each Fe1−W bond length from 2.1 (bonding) to 2.6 Å (nonbonding distance) change the energy by ∼3kcal, indicating a relatively flat potential energy surface for this range of bond lengths. To further explore the effect of water ligation on the energies of the biferrous center in MmoH, each Fe−W bond was constrained to 2.6 Å while allowing the second Fe−W and surrounding structure to optimize. In all cases the unconstrained water bond was strengthened, compensating for the nonbonding water. The 2.6 Å Fe−W$_{axial}$ structure is ∼1 kcal lower in energy than the resting structure, while the 2.6 Å Fe−W$_{eq}$ structure is 1.5 kcal higher in energy, suggesting it may be energetically favorable for the axial water to remain unbound.

Upon removal of the Fe−W bond constraint, reoptimization of the structure with a long Fe−W$_{eq}$ distance results in the original resting structure. Optimizations starting with the axial water at 2.6 Å or greater from Fe1 results in resting structure II (Figure 9, bottom). This structure is 7 kcal lower in energy than

(53) Noodleman, L. *J. Chem. Phys.* **1981**, *74*, 5737–5743.
(54) Rosenzweig, A. C.; Brandstetter, H. W.; Whittington, D. A.; Nordlund, P.; Lippard, S. J.; Frederick, C. A. *Proteins* **1997**, *29*, 141–152.

relative to resting structure I and has a final W$_{axial}$ distance of 2.9 Å (Table 2). A hydrogen-bonding network of two additional water atoms links the axial water to Leu110 and appears to be responsible for this movement. The unbound W$_{axial}$ is centered below the two Fe's and also hydrogen bonds with Glu 209 on Fe2 as shown at the bottom of Figure 9, affording a smaller Fe−Fe−O$_{(Glu209)}$ angle of about 94°. As described below, resting structure II has two 5 coordinate irons and is in better agreement with the spectroscopy as its ligand field splitting is also more consistent with the CD/MCD spectra. Bond distances and angles are in good agreement with the crystallography, except for the Fe1−Fe2−Glu209 angle that is about 25° smaller than in the crystal structure. It has been noted that flexibility in carboxylate ligands can play an important role in reactivity[4] and as this ligand also shows disorder within the crystal structure its position was systematically explored as described below.

2. Ligand Field Description of the Resting State. The splitting pattern of the d-orbital manifold provides insight into the geometric and electronic structure of each Fe(II). Analysis of the T4moH CD/MCD transitions assigned one iron to the inner, closely spaced transitions in Figure 2 at 7200 and 8600 cm^{-1}, while the second iron shows much greater splitting with one transition at 5300 cm^{-1}, lower than the inner transitions, and one higher at 10 500 cm^{-1}. This same pattern is observed in MmoH spectra, assigning two inner transitions at 7500 and 9000 cm^{-1} to one iron, and the higher energy transition at ∼10 000 cm^{-1} assigned to other, while the corresponding low energy transition is assumed to be below the detection limit of the instrument. Both irons are 5 coordinate and ferromagnetically coupled.[1] Neither the experimentally observed splitting pattern of the inner-outer transition pairs nor the assignment of two five coordinate irons agree with the DFT optimized 6C,5C MmoH resting structure I (Figure 9, top) as can be seen in the d-orbital energy splittings shown in Figure 10, left black. Movement of the axial water to form resting structure II, with two 5 coordinate irons and a Fe−Fe−Glu209 angle of 94°, shows a splitting pattern in closer agreement (red structure and splittings in Figure 10). However, the Fe−Fe−Glu209 angle must be increased to 114°, within 5° of the crystallographically determined angle, to reproduce the spectroscopically observed inner and outer pairs of transitions. This final optimization to resting structure III (Figure 10, green) is ∼5 kcal higher in energy than resting structure II (red) however still lower in energy than the 6C/5C resting structure I, and is in good agreement with crystallographic and spectroscopic data (Table 2).

The percentage contributions from the d-orbitals (d$_{xy}$, d$_{xz}$, d$_{yz}$, d$_{z^2}$, d$_{x^2−y^2}$) to each molecular orbital for both Fe's are given in Table 4, using the local coordinate system shown for each Fe in Figure 11. For resting structures II and III, the local coordinate systems remain the same and the major contributor to each of the d-orbitals is labeled above its respective energy level at the top of Figure 10 (red/green). As shown in Figure 11A, the z-axis of Fe1 lies directly along the Fe1−O$_{Glu114}$ bond and the Fe1−W$_{eq}$ bond is along the x-axis. The highest energy d-orbital on Fe1 has 87% d(z^2) character (orbital shown in Figure 11A, right), consistent with a trigonal bipyramidal geometry. However, the Fe−O$_{Glu243}$ bond is tilted off the z-axis by ∼25°, lowering the energy of the d(z^2) transition and mixing it with the other orbitals. A large, 148°, W$_{eq}$−Fe1−O$_{Glu144}$ angle in the equatorial plane decreases the W$_{eq}$−Fe1−N$_{His147}$ angle to nearly 90°, providing strong overlap of the d($x^2−y^2$) orbital with the short Fe−W$_{eq}$ and Fe−N$_{His147}$ bonds, thus raising its energy.
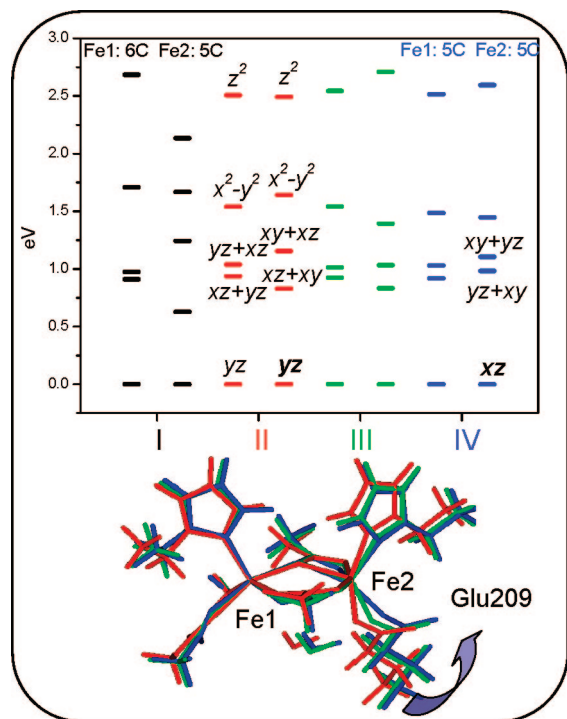
Figure 10. (Top) Plot of the Fe1 (left) and Fe2 (right) d-orbital energy splittings for each structural perturbation: 5C/6C resting structure (black) 5C/5C resting structure (red), 5C/5C resting with Fe—Fe—Glu angle of 114° (green), 5C/5C component B perturbed structure with Fe—Fe—Glu angle of 135° (blue). Orbitals are labeled based on their major composition, shown in Table 4 (orbital compositions for structures II, III, and IV are identical except where noted). (Bottom) Optimized structures of each perturbation in respective color showing the proposed effect of component D/B.

The wide W_{eq}—Fe1—O_{Glu144} angle also provides an open binding site that can be utilized in the O_2 reaction of the diiron site. These distortions significantly decrease the energy splitting of the ligand field excited states for Fe1, allowing this iron to be correlated with the 'inner' set of paired transitions observed in the CD/MCD spectra.

The local coordinate system on Fe2 aligns the z-axis along the Fe2—O_{Glu144} bond. The $d(z^2)$ orbital overlaps very strongly with this bond, and weakly with the nonbridging oxygen of Glu243 shown in Figure 11B, right. The x-y plane contains the Fe2—N_{His246} bond, the slightly weaker Fe2—O bond from the nonbridging oxygen of Glu243, and the Fe2—O_{Glu209} bond. However, the smaller Fe—Fe—$O_{(Glu209)}$ angle of about 114° shifts this bond out of the x-y plane. This mixes a larger percentage of $d(x^2-y^2)$ character into the highest energy $d(z^2)$ orbital (Table 4B), indicative of greater distortion toward a square pyramidal from its trigonal bipyramidal structure than for Fe1. This results in a greater splitting between the $d(z^2)$ and $d(x^2-y^2)$ orbitals, thus Fe2 can be correlated with the outer set of experimentally observed ligand field transitions. Consequently both iron sites in the final resting structure are described as distorted trigonal bipyramidal sites with a greater distortion toward square pyramidal on Fe2, consistent with the spectroscopic data.

B. Component B/D Effect. From the spectral data for both MmoH and T4moH, the outermost peaks, now assigned to Fe2, are most strongly perturbed upon binding of their effector proteins. The hydrogen bonding networks within MmoH and modeling studies on effector protein binding have suggested that His246 and Glu209 on Fe2 are most likely to be affected upon complex formation.[21,35,37] Variability in the position of

Table 4. Relative Energies, E_{rel} (eV), and Percentage Contributions to Relevant Fe(II) d-Based Molecular Orbitals Based on the Coordinate Systems Shown in Figure 11 and Obtained from C-Squared Population Analysis of Broken-Symmetry Calculations on Reduced MMOH Structures

(A) Spin-down MO, localized at Fe1 in resting structure							
level	E_{rel} (eV)	z^2	x^2-y^2	xy	xz	yz	total
			unoccupied				
214	2.54	87	5	2	0	0	94
212	1.54	6	77	0	1	1	85
209	1.02	8	0	60	0	2	70
208	0.93	3	1	0	55	21	80
			occupied				
204	0	1	3	1	27	58	90

(B) Spin-down MO, localized at Fe2 in resting structure							
level	E_{rel}(eV)	z^2	x^2-y^2	xy	xz	yz	total
			unoccupied				
215	2.71	90	8	0	1	0	99
213	1.39	8	72	0	1	2	83
211	1.03	0	1	49	18	7	75
209	0.83	1	5	17	47	0	70
			occupied				
205	0	1	8	6	1	75	91

(C) Spin-down MO, localized at Fe2 in perturbed structure							
level	E_{rel}(eV)	z^2	x^2-y^2	xy	xz	yz	total
			unoccupied				
215	2.59	77	4	1	0	0	82
213	1.45	6	70	1	0	6	83
212	1.11	2	5	40	0	16	63
211	0.983	5	15	28	8	31	87
			occupied				
205	0	0	3	5	74	7	89

these ligands, particularly Glu209, in the crystal structures and the flexibility of the surrounding protein environment allow this carboxylate ligand to shift upward, increasing the Fe—Fe-Glu209 angle. This flexibility was also noted in the optimized resting structures (II, red and III, green in Figure 10) described above. Movement of this ligand has little effect on the overall optimization of the structure, however it results in a large change in the ligand field of Fe2 (Figure 10) while Fe1 is only slightly perturbed. This same trend is observed in the CD/MCD data for both proteins.

Optimization of the green resting structure while constraining the Fe—Fe—Glu209 angle to 135°, gives structure IV (blue structure and energy level splitting shown in Figure 10, right) at 9 kcal higher in energy than resting structure III. The geometry and bond lengths of the Fe1 center remain unchanged, thus the ligand field splitting pattern and orientation of the redox active orbital on Fe1 are unperturbed. The ligand field splitting on Fe2 narrows, however, due to a decrease in the energy of the $d(z^2)$ orbital and an increase in the $d(x^2-y^2)$ energy as the Fe—O_{Glu209} bond is shifted into the $x-y$ plane and aligned more closely with the y-axis (Figure 11C). As seen in Table 4C, this distortion decreases the amount of $d(x^2-y^2)$ character mixed into the $d(z^2)$ orbital as the geometry of the Fe2 center becomes less distorted toward square pyramidal and more similar to Fe1. The calculated perturbation is similar to that observed experimentally with binding of T4moD/MmoB to T4moH/MmoH and correlates the component D/B effect with a shift in Glu209 on Fe2. This shift in Glu209 also rotates the orientation of the HOMO on Fe2, its redox active orbital, from $d(yz)$ to $d(xz)$
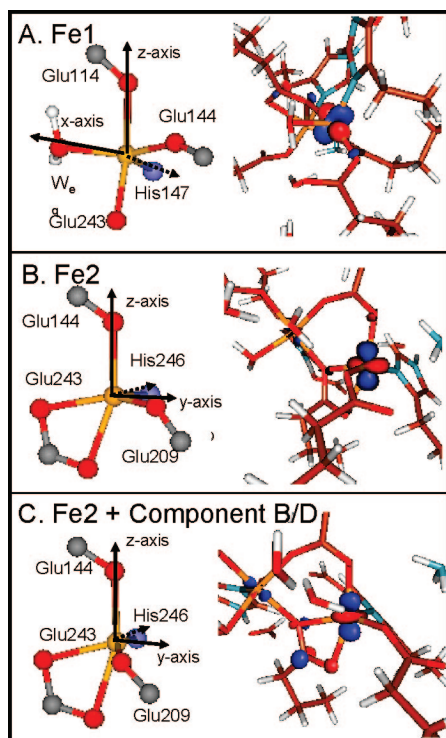
Figure 11. Axis systems defined by major composition of d-orbital (A) Fe1 from resting structure III with Fe−Fe−Glu angle of 114° (B) Fe2 from same resting structure (C) Fe2 from component B perturbed structure with Fe−Fe−Glu angle of 135° (blue structure in Figure 10). Fe1 from this structure is not shown, as there is negligible change to the d-orbital manifold and axis system.

(Table 4). The significance of this structural change and orbital rotation is discussed below.

Discussion

I. Spectroscopy and DFT of the Resting Site: Comparison to Crystallography. T4moH and MmoH share many similarities including conservation of the binuclear motif through retention of key residues associated with the iron ligands.[5,6,37] CD/MCD studies of T4moH and MmoH have found the active sites of both monooxygenase systems to be almost identical and similarly perturbed by their effector proteins. Figure 12, top, shows the overlay of CD (left) and MCD (right) spectra for MmoH and T4moH. In the CD spectrum of MmoH, two negative bands are observed near 7200 and 9900 cm^{-1}. These transitions could obscure the presence of an additional band, and in the CD spectrum of T4moH a third positive band around 8500 cm^{-1} can now be resolved between the two negative transitions. In the MCD data, these three transitions are now cleanly observed in MmoH and T4moH, while an additional band at 5300 cm^{-1} is observed in T4moH. Therefore a total of 4 bands are present in the combined spectra. In each species, the inner d-d transitions around 7000 and 8500 cm^{-1} have been assigned to Fe1 and the corresponding VTVH data are best fit with the larger negative D value. In MmoH, the high-energy peak around 10 000 cm^{-1} was assigned to Fe2 and thought to be paired with a low energy peak that was not observed but presumed to be present below the detection limit. This low energy band is now clearly resolved at 5300 cm^{-1} in the T4moH spectrum, and thus the outer transitions around 10 000 and 5000 cm^{-1} can both be assigned to Fe2, with the smaller negative D value. Both Fe's are 5 coordinate trigonal bipyramidal and found

to be ferromagnetically coupled, consistent with the presence of a $\mu-1,1$ bridging carboxylate in each monooxygenase.

Although an active site structure of T4moH is unavailable, crystal structures of MmoH have been solved for multiple crystallization conditions. Although there are variations in structure between different redox states, the diiron site in the reduced form is consistently bridged by Glu243 in a $\mu-1,1(\eta^1\eta^2)$ fashion, with bidentate coordination to Fe2.[5,6] This is consistent with the small positive J (exchange coupling) obtained from VTVH MCD analysis of T4moH and MmoH.[1] However, inconsistent with the spectroscopy and among crystal structures is the number of bound waters on Fe1,[5,54] making this center either 5 or 6 coordinate. Density functional studies based on these crystal structure coordinates found that resting structure I shown in Figure 9, which optimized to one 5 coordinate and one 6 coordinate iron, is 7 kcal/mol higher in energy than resting structure II, in which the axial water opposite His147 is completely dissociated from Fe1 leaving two 5 coordinate irons. Finally, comparison of the d-orbital splitting patterns (Figure 10) for each of the structures shows that resting structure III, in which the Fe−Fe−Glu209 angle is increased from 94° (resting structure II) to 114°, is most consistent with the CD/MCD and crystallographic data. In this structure both irons have trigonal bipyramidal ligand fields, with Fe2 more distorted toward square pyramidal while maintaining the $\mu-1,1$ bridged Glu243.

For this resting site to react with dioxygen to form the spectroscopically observed peroxo bridged intermediate,[55] one electron from each iron of the biferrous center must be transferred to the half-occupied antibonding π^* orbitals of dioxygen. Two possible scenarios for this type of reaction have been explored in previous computational studies.[8,56,57] The first involved dioxygen binding to a single Fe at the biferrous center. One electron was transferred from the bound Fe to form a superoxide that was higher in energy than the resting state plus O_2. The resultant Fe(III) superoxide formed a weak bond, making this reaction thermodynamically unfavorable. Importantly, the poor superexchange pathways offered by the bridging carboxylate ligands in the diiron site do not facilitate transfer of the additional electron from the second Fe necessary to form the more stable peroxo species. The alternative scenario considered dioxygen reacting in a bridging mode at the biferrous site. This allowed one electron to be transferred from each fully occupied Fe(II) HOMO to one of the half-filled O_2 orbitals forming the significantly more stable peroxo species. In this case, the peroxide binds strongly to the two Fe(III)'s, providing the thermodynamic stabilization necessary to drive the reaction.

In MmoH, this energetically favored pathway would require open coordination positions on both irons in the correct orientation for dioxygen to bridge. The wide $W_{eq}-Fe1-O_{Glu144}$ angle on Fe1 in resting structure III (green, Figure 10) provides a site available for O_2 binding oriented toward the second iron. In either 5C,5C resting structure, however, overlaying Van der Waals radii shows that the position of Glu209 eliminates any open coordination position on Fe2 and thus sterically hinders dioxgyen from bridging the two Fe's to form the more stable peroxo intermediate. The orientation of the available redox

(55) Liu, K. E.; Wang, D. L.; Huynh, B. H.; Edmondson, D. E.; Salifoglou, A.; Lippard, S. J. *J. Am. Chem. Soc.* **1994**, *116*, 7465–7466.
(56) Wei, P.; Skulan, A. J.; Wade, H.; DeGrado, W. F.; Solomon, E. I. *J. Am. Chem. Soc.* **2005**, *127*, 16098–16106.
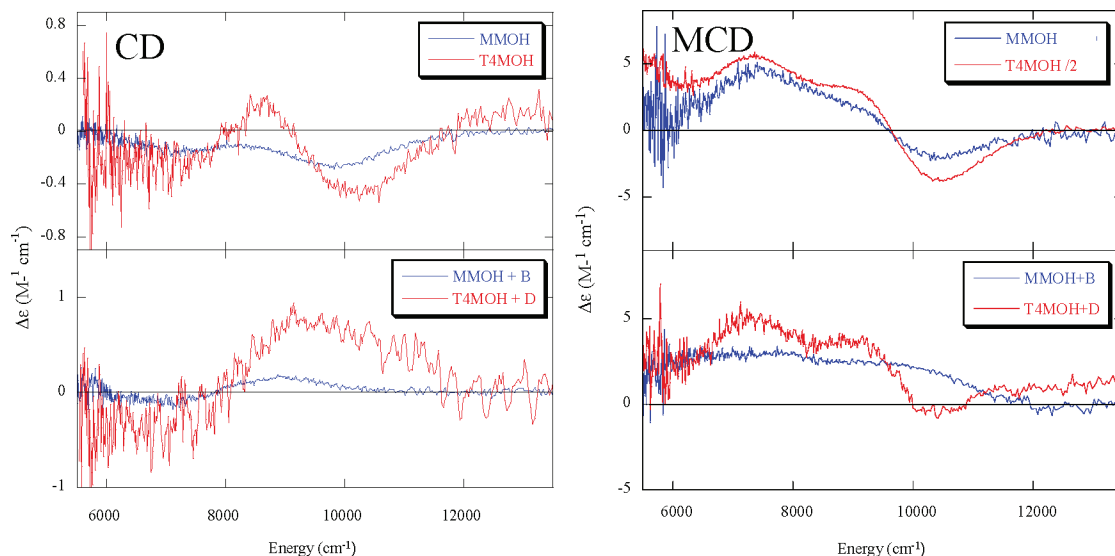(57) Schenk, G.; Pau, M. Y. M.; Solomon, E. I. *J. Am. Chem. Soc.* **2004**, *126*, 505–515.

Figure 12. (Top) CD and MCD spectra of MMOH (blue) and T4MOH (red). (Bottom) CD and MCD spectra of MMOH+MMOB (blue) and T4MOH+ T4MOD (red). CD spectra recorded at 5 °C and MCD spectra recorded at 1.6 K, 7 T.
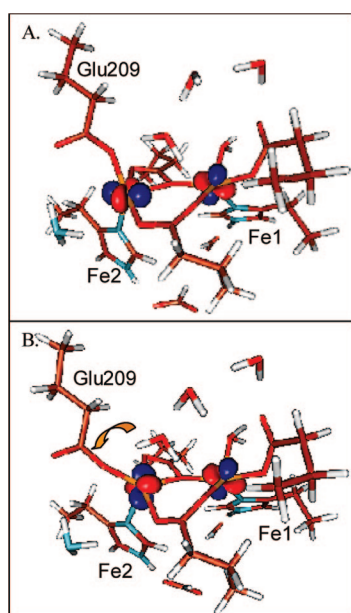

Figure 13. Surface plots of the highest occupied spin-up MO's on each Fe(II) obtained from BS calculations. (A) Resting structure and (B) proposed Component B perturbation.

active orbitals on each iron can also play a role in the reaction coordinate of intermediate formation. In the MmoH resting site these are not oriented for optimal overlap with the dioxygen acceptor orbitals (Figure 13A, vide infra). Thus, the inability of dioxygen to bridge the Fe's as well as the poor alignment of their redox active orbitals limit efficient O_2 reactivity of the resting site.

II. Spectroscopic and Computational Elucidation of the Component B/D Effect: Implications for Oxygen Reactivity. As detailed in the Introduction, the interaction of component D/B with the hydroxylase component has been proposed to serve two functions: controlling site accessibility and activating the site for O_2 reactivity.[28] Although several modeling studies have given insight into the gating effects of T4moD/MmoB, less is known about the changes that occur at the active site. CD and MCD spectra reveal that formation of these complexes results

in similar spectral perturbations in both species, reflecting a change in geometry of the active site. From the MmoH+MmoB spectra shown in blue in the bottom plots of Figure 12, it is evident that the outer peaks associated with Fe2 are most greatly perturbed as the transition at 10 000 cm^{-1} changes sign in MCD (Figure 12, bottom right, blue) and a peak at 5500 cm^{-1} is now present, having shifted to a higher energy.[1,27] In T4moH+T4moD the low energy transition already present at 5300 cm^{-1} and the higher energy band at 10 500 cm^{-1} are also most affected, showing a large decrease in MCD intensity. The two inner bands around 7000 and 8500 cm^{-1}, associated with Fe1, remain relatively unperturbed in both spectra. Although past MmoH studies have not specifically defined the effect of MmoB on the active site, some computational work has considered the removal of the axial water ligand from Fe1 to be the primary step before O_2 reactivity.[58,59] However, these CD/MCD studies of T4MO and sMMO indicate the perturbation primarily affects the geometry of Fe2, and clearly rule out a change in coordination number of either Fe as the effect of component D/B on the active site.

Several of the amino acid residues bound to Fe2, including Glu209, Glu243, and His246, are at the end of a hydrogen-bonding network extending from the proposed binding position of MmoB,[17] suggesting these ligands may be able to contribute to the change in this Fe center. Analyses of the VTVH MCD data show that the $\mu 1,1$ bridging mode of Glu243, which has been suggested to change due to shifts seen between redox states,[5] must remain intact in the biferrous state although minor movement of this ligand is seen during DFT optimizations. Because the sites remain ferromagnetic after binding of the effector proteins, a $\mu 1,1(\eta^1\eta^2)$ bridging mode must also be present in the biferrous component D/B perturbed structures. Glu209, however, also shows disorder in the crystal structures[5,7,54] and a large range of flexibility in the Fe−Fe−Glu209 angle was observed during DFT optimizations. Additionally, the steric problems of Fe1−O_2 bridging to Fe2 that were discussed above for the resting structure, are associated with the position of Glu209 between the two Fe centers. For these reasons, Glu209

(58) Gherman, B. F.; Baik, M. H.; Lippard, S. J.; Friesner, R. A. *J. Am. Chem. Soc.* **2004**, *126*, 2978–2990.

(59) Yoon, S.; Lippard, S. J. *J. Am. Chem. Soc.* **2005**, *127*, 8386–8397.

seemed the most likely ligand to contribute to the component D/B effect on the biferrous active site of the hydroxylase component.

In the related enzyme stearoyl-ACP Δ^9 desaturase, site-directed mutagenesis and computer docking studies have implicated binding of [2Fe-2S] ferredoxin to the surface residue Lys230, which is on the same helix, and immediately adjacent in the amino acid sequence to Glu229, the comparable residue in the desaturase to Glu209 in MmoH.[60] It is plausible that interactions between desaturase, ferredoxin and acyl-ACP result in similar rearrangements in the desaturase as proposed here for the diiron hydroxylases upon binding effector proteins.

DFT calculations find that movement of the Fe−Fe−Glu209 angle from 114° (resting structure III) to 135° (structure IV) reproduces the changes in the ligand field of Fe2 seen in the CD/MCD spectroscopy upon binding of the effector proteins (Figure 10). The transition to $d(x^2-y^2)$ on Fe2 increases in energy explaining the appearance of the low energy transition now present in the MmoH-MmoB spectrum and altered in the T4moH-T4moD spectrum. This, coupled with a decrease in the energy of the $d(z^2)$ orbital, tightens the splitting in the outer (Fe2) transitions while the splitting on Fe1 is negligibly perturbed (Figure 10, IV/blue).

This optimized structure is consistent with the spectroscopy of the T4moD/MmoB perturbed active sites that have been found to be more reactive with dioxygen. Both irons remain in 5-coordinate trigonal bipyramidal geometries and are bridged in a $\mu-1,1$ mode by Glu243. The larger Fe−Fe−Glu209 angle opens a coordination position on Fe2 that is oriented toward the open site on Fe1, allowing dioxygen to bridge the site without steric interference. This allows each iron to transfer one electron to dioxygen, leading to a peroxide bridge that forms stronger donor bonds to each of the resultant ferric centers. A second contribution to the reaction coordinate is the correct alignment of the Fe(II) HOMOs that must interact with the half-filled π^* dioxygen orbitals. These dioxygen orbitals are perpendicular to each other and thus require the redox active orbital of one Fe(II) to be aligned for σ overlap along one of the Fe−O bonds (π^*_σ) while the second must then provide π overlap (π^*_ν). Both redox orbitals of the resting structure are d(yz) orbitals oriented for sigma overlap along the potential Fe−O bonds (Figure 13A). This would result in the transfer of two electrons into the π^*_σ orbital, requiring spin pairing of the two oxygen electrons in π^*_ν early in the reaction coordinate.[8] Shifting Glu209 rotates the HOMO on Fe2 from d(yz) to d(xz), correctly orienting it for pi overlap with the π^*_ν oxygen orbital while the d(yz) HOMO that is maintained on Fe1 provides good sigma overlap with the π^*_σ (Figure 13B). These strong overlaps facilitate efficient 2-electron transfer, one from each iron, contributing to the increased reactivity at the component D/B perturbed active site. Structures and energetics of possible peroxo intermediates will be further explored in future studies.

In summary, spectroscopy of T4moH and T4moH+T4moD gives parallel results to those obtained on MmoH and MmoH+MmoB. The data clearly show two sets of two ligand field transitions indicative of two inequivalent 5 coordinate irons, one of which is perturbed upon complexation with the effector protein. DFT calculations on the MmoH crystal structure further clarify that the effect of binding T4moD/MmoB to T4moH/MmoH is not to remove a water ligand from either iron but to induce a change in orientation of the terminal glutamate on Fe2. This would allow O_2 to bridge the diiron site and aligns the redox active orbital on each Fe for efficient 2-electron transfer, facilitating the formation of a stabilized peroxo intermediate. These results give insight into both the effect of the D/B coupling protein on activating T4moH and MmoH for catalysis, and structural features of the nonheme biferrous active site that may be necessary for O_2 reactivity.

Supporting Information Available: Cartesian coordinates of each final optimized structure. This material is available free of charge via the Internet at http://pubs.acs.org.

JA800654D

(60) Sobrado, P.; Lyle, K.; Kaul, S.; Turco, M. M.; Arabshahi, I.; Marwah, A.; Fox, B. G. *Biochemistry* **2006**, *45*, 4848–4858.